Optical pulling force arising from nonparaxial accelerating beams

Hao Wu,[1] Xuejing Zhang,[1] Ping Zhang,[1] Pengbo Jia,[1] Zhaoyuan Wang,[1] Yi Hu,[1,*] Zhigang Chen,[1,2] and Jingjun Xu[1,†]

[1]*The MOE Key Laboratory of Weak-Light Nonlinear Photonics, TEDA Applied Physics Institute and School of Physics, Nankai University, Tianjin 300457, China*

[2]*Department of Physics and Astronomy, San Francisco State University, San Francisco, California 94132, USA*

(Received 29 December 2020; revised 18 March 2021; accepted 26 April 2021; published 13 May 2021)

We study the optical forces experienced by a dielectric microsphere placed in a nonparaxial vector self-accelerating beam. Following the beam's peak intensity (or the main lobe), where the dominant transverse trapping appears, the longitudinal optical force is found to switch from a purely pushing case to an impure case involving pulling forces. The pulling forces tend to appear away from the optimal transverse trapping position, particularly for large particles but populate largely within the transverse trapping potential. In terms of magnitude, such forces can be comparable to the transverse ones when manipulating small particles. The cases of both Mie and Rayleigh particles are discussed. Our work opens the possibility to uncover the pulling effect in nonparaxial accelerating beams, which may lead to applications in optical trapping and manipulation.

DOI: 10.1103/PhysRevA.103.053511

I. INTRODUCTION

Self-accelerating beams can propagate along curved paths with preserved intensity profiles in free space [1,2]. Such an intriguing feature is imparted through a proper shaping on the wavefronts of optical beams. The peculiar momenta stored in the structured light can be transferred to other entities by means of interactions, such as electrons, nonlinearly induced dipoles, and microparticles [3–11], leading to a variety of exotic phenomena and potential applications. In optical manipulation, this kind of momenta was first utilized for particle clearing [3], resorting to the Airy beams [12,13] (i.e., the first type of self-accelerating waves demonstrated in optics). Following this pioneering work, extensive studies were performed to analyze the force distributions of a particle placed in an Airy beam or their ramifications, aiming to improve particle trapping and delivery [14–28]. Under the nonparaxial condition commonly encountered in a microscope system setup for optical tweezers, paraxial accelerating beams represented by Airy beams face difficulties in realizing a sharp bending. To overcome this limitation, nonparaxial accelerating beams [29–38] were conceived, allowing for particle delivery to distances at steeper angles [39]. However, to the best of our knowledge, no force analysis has been performed for these nonparaxial beams. In particular, considering that nonparaxial accelerating beams are endowed with quite large momenta (i.e., theoretically, these beams can turn 90 degrees during propagation), optical pulling effects that have recently attracted lots of attention [40] are highly expected, inspired by counterintuitive manipulations via various structured optical beams [41–49] that can pull the scatterers along a direction even opposite to the beam propagation, often called "tractor beams" [50].

In this paper, we study theoretically optical forces exerting on a dielectric microsphere for nonparaxial accelerating beams. Our results show that the beam components of a nonparaxial vector accelerating beam around the peak intensity (or the main lobe) produce the dominant trapping capability. The associated trapping potential has an asymmetric distribution pertinent to the beam asymmetry along the acceleration direction, leading to a location mismatch for the peak intensity and the optimal transverse trapping position. Surprisingly, in the transverse trapping regions around the peak intensity, the longitudinal optical force is found to switch sign during propagation, from a purely pushing type to a combination of pushing and pulling types. The pulling force appears between the main lobe and the nearby sublobe, particularly for large particles. It can be comparable to the transverse force in terms of strength for a beam that bends strongly or for the manipulation of a small particle. Our work paves the way for experimental realization of the optical pulling effect via nonparaxial accelerating beams, which has not been explored and observed yet.

II. NONPARAXIAL VECTOR ACCELERATING BEAMS

We begin our analysis by considering that a vector electromagnetic (EM) field, with the suppressed time dependence $e^{-i\omega t}$ throughout this paper, propagates along the positive z direction. By utilizing the method of vector angular spectral decomposition [51] that describes rigorously the vector EM fields of an arbitrary beam, the evolution of the electric field in a nonmagnetic isotropic medium is expressed as

$$\mathbf{E}_{\mathrm{inc}}(x,y,z)=\iint_{-\infty}^{\infty}\tilde{\mathbf{A}}(k_x,k_y)e^{i(k_x x+k_y y+k_z z)}dk_x dk_y, \quad (1)$$

*yihu@nankai.edu.cn
†jjxu@nankai.edu.cn

 ©2021 American Physical Society

where k_x, k_y, and k_z are the wave vectors satisfying the relation $k^2 = k_x^2 + k_y^2 + k_z^2$. They are reformulated as $k_x = k\sin\alpha\cos\beta$, $k_y = k\sin\alpha\sin\beta$, and $k_z = k\cos\alpha$ in spherical coordinates in which $\alpha(\beta)$ is the polar (azimuthal) angle. $k = \frac{2\pi n_b}{\lambda}$ represents the wave number with n_b and λ denoting the refractive index of the background medium and the light wavelength in vacuum, respectively. $\tilde{\mathbf{A}}(k_x, k_y)$ is the vector angular spectrum function that has a form of

$$\tilde{\mathbf{A}}(k_x, k_y) = \frac{E_0}{4\pi^2} A(k_x, k_y)\mathbf{Q}(\alpha, \beta), \tag{2}$$

where E_0 is the amplitude of the electric field, $A(k_x, k_y)$ contributes to the profile of the incident beam (i.e., at $z = 0$) [52], and $\mathbf{Q}(\alpha, \beta)$ is a complex vector function defining the light polarization in the following form [52]:

$$\mathbf{Q}(\alpha, \beta) = \begin{bmatrix} p_x(\cos\alpha\cos^2\beta + \sin^2\beta) - p_y(1-\cos\alpha)\sin\beta\cos\beta \\ -p_x(1-\cos\alpha)\sin\beta\cos\beta + p_y(\cos\alpha\sin^2\beta + \cos^2\beta) \\ -p_x\sin\alpha\cos\beta - p_y\sin\alpha\sin\beta \end{bmatrix} \begin{Bmatrix} \mathbf{e}_x \\ \mathbf{e}_y \\ \mathbf{e}_z \end{Bmatrix}, \tag{3}$$

where p_x and p_y correspond to the polarization regime of the incident beam, and $\mathbf{e}_x$, $\mathbf{e}_y$, $\mathbf{e}_z$ are the unit vectors of a Cartesian coordinate system. Accordingly, the incident magnetic field is

$$\mathbf{H}_{\text{inc}}(x, y, z) = \frac{1}{i\omega\mu}\nabla \times \mathbf{E}_{\text{inc}}(x, y, z), \tag{4}$$

where ω is the angular frequency and μ is the permeability of the background medium. For a type of nonparaxial vector accelerating beam (NVAB) that undergoes shape-preserving propagation along a semicircular trajectory [36], its associated vector angular spectrum function is

$$\tilde{\mathbf{A}}(k_x, k_y) = \frac{E_0}{4\pi^2} g(t)\exp(im_a f)\mathbf{Q}(\alpha, \beta), \tag{5}$$

where t and f are related to the wave vector (k_x, k_y) by $t = \arccos(\frac{k_y}{k})$ and $f = \arcsin(\frac{k_x}{\sqrt{k_x^2+k_z^2}})$, respectively, and m_a is a positive real number used to design the beam trajectory with a beam radius close to $\frac{m_a}{k}$. Indeed, any form of $g(t)$ corresponds to an NVAB. To directly compare with the optical-tweezer effect via Airy beams, we examine herein the NVAB having an Airy-like intensity profile. In this regard, a form of $\frac{1}{2\pi\sin t}$ is adopted for $g(t)$. The initial polarization is set in terms of experimental consideration. In general, a liquid-crystal-based spatial light modulator is employed to produce the nonparaxial accelerating beams [53] by modulating the light in the domain of spatial frequency. Considering the polarization-dependent feature of a liquid crystal, we set the polarization of the light illuminating the modulator along one direction (here the x axis). In this framework, the vector angular spectrum function of the associated beam becomes

$$\tilde{\mathbf{A}}(k_x, k_y) = \frac{E_0\exp(im_a f)}{8\pi^3\sin t} \begin{bmatrix} \cos\alpha\cos^2\beta + \sin^2\beta \\ (\cos\alpha - 1)\sin\beta\cos\beta \\ -\sin\alpha\cos\beta \end{bmatrix} \begin{Bmatrix} \mathbf{e}_x \\ \mathbf{e}_y \\ \mathbf{e}_z \end{Bmatrix}. \tag{6}$$

Note that the phase term in Eq. (6) does not include any spiral phase. Thus, in the following analysis, we do not consider optical effects associated with rotations. Substituting Eq. (6) into Eq. (1), the electrical field distribution of the NVAB is readily obtained. Figure 1 illustrates the associated intensity profiles. The parameters for the calculations are chosen as $E_0 = 1$, $m_a = 200$, $n_b = 1.33$ (water), and $\lambda = 532.8$ nm. The NVAB shows a shape-preserving evolution along an arc. As mentioned before, its transverse profile exhibits a pattern [Fig. 1(b)] similar to that of Airy beams [12,13], consisting of a main lobe carrying the peak intensity and various sublobes necessary for the beam acceleration. In essence, this beam is mainly contributed by the x- and z-polarized components that dominate the initial and final beam propagation, respectively. In transverse planes, both parts show an Airy-like structure. In the following, based on the full-wave generalized Lorenz-Mie theory and the Maxwell stress tensor technique (see details in the Appendix), we calculate the optical force exerted by the NVAB on a Mie particle or a Rayleigh particle. Note that, unless otherwise stated, the power of the incident NVAB is set to be $P = 20$ mW, corresponding to $E_0 \approx 2.17 \times 10^{-5}$ V/m. We choose this power as a typical example. This will not cause loss of generality since the calculated force is, in general, proportional to the light power.

III. OPTICAL FORCE ON A DIELECTRIC MICROSPHERE

In this section, we first investigate the optical force of the NVAB exerting on a Mie particle positioned in water [see Eq. (A9) in the Appendix]. The particle is made of polystyrene. Its radius r_s, permittivity ε_s, and mass density are 0.4 μm, 2.53, and 1050 kg/m^3 [42], respectively. In our analysis, the force due to gravity (about 2.76 fN; much smaller than the optical force exerted by the NVAB) is ignored.

To overview the force distribution, the calculation is initially performed in a transverse plane at $z = 10/k$. Figure 2(a) presents the transverse component $\mathbf{F}_\perp$ [$|\mathbf{F}_\perp| = (F_x^2 + F_y^2)^{1/2}$] (see details in the Appendix) in this plane. The lobes with sufficient intensity can trap the particle transversely. As expected, the main lobe offers the dominant trapping effect. The trapping position in the main lobe is close to the location of the peak intensity. In addition, the longitudinal optical force F_z is examined along the beam acceleration direction (i.e., the x axis). As shown in Fig. 2(b), the particle always experiences a pushing force whose maximum value nearly appears at the location of the peak intensity. Thus, in the plane at $z = 10/k$, once the particle is trapped by the main lobe or the sublobes, it tends to move along the beam trajectory. This is also the case for other planes in early propagations, where the beam just manifests a small bending.

Once the beam turns into a large angle, the longitudinal optical force can become negative. As an example, F_z is analyzed following the peak intensity along the propagation, and the associated calculations are summarized in Fig. 3. In the

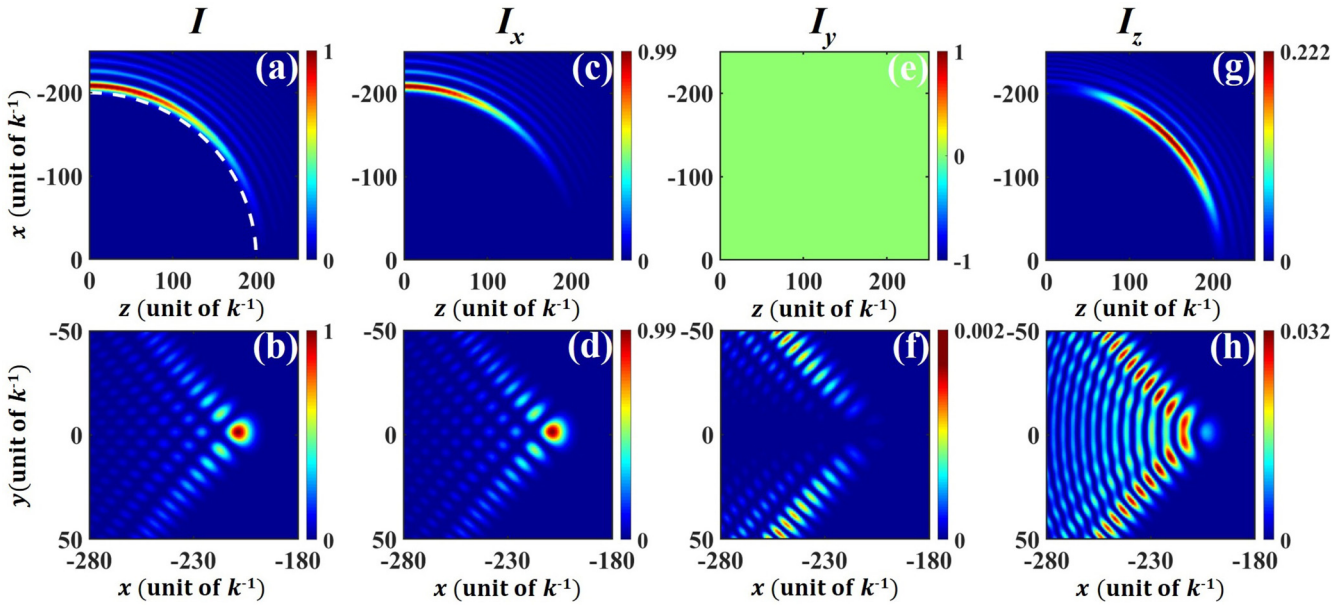

FIG. 1. Intensity profiles of the NVAB under test. Shown from left to right are the total intensity pattern and its three polarized components. Upper and lower rows are the cases at a longitudinal section (at $y = 0$) and a transverse section (at $z = 0$), respectively. The white dashed curve in panel (a) traces out the beam trajectory. Each panel is normalized by the peak intensity.

range $0 \leqslant z < 115/k$, F_z is positive, with the maximum value appearing at the input, while in the range of $115/k \leqslant z < 200/k$, it becomes negative with the minimum value appearing around $z = 160/k$ [Fig. 3(a)]. To have a better illustration, the forces are plotted in Fig. 3(b) by means of arrows overlapped with the pattern of the beam propagation. One can see a clear switching of the force type following the peak intensity. For quite large bending of the beam, the pulling strength is alleviated because of the reduced peak intensity.

The optical pulling force is strongly related to the wave-vector direction [43,50]. To better understand its origin, the optical rays passing through a tiny space around the peak intensity are examined. They are initiated from the Fourier plane, and their paths in real space are determined by the phase of the angular spectrum [i.e., Eq. (6)] [54]. Figures 4(a) and 4(b) present the k-space locations of the rays passing through two sites A and B marked in Fig. 3(b), selected by considering that the associated longitudinal optical forces oppose each other and reach the maximum strength beneficial for a sharp comparison. Clearly, the optical pulling effect is relevant to the beam components of high spatial frequency. Furthermore, the momentum distributions are transformed into ray angles about the z axis, as shown in Figs. 4(c) and 4(d). Around site A, the ray angles are in the range of $15.75^\circ \leqslant \alpha \leqslant 17.19^\circ$; while around site B, quite larger angles are involved, and the maximum value reaches $\approx 67^\circ$. These wave vectors, in the latter case, have a small projection along the propagation direction, thereby leading to an enhancement

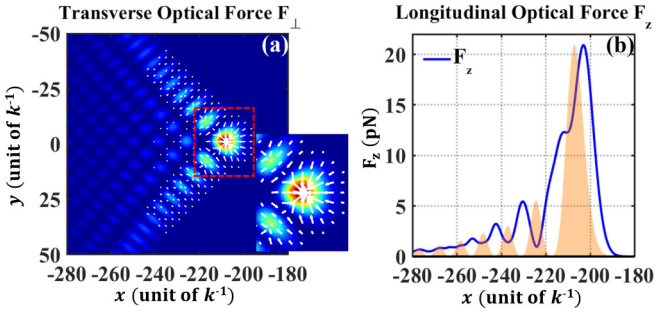

FIG. 2. (a) Transverse optical force experienced by a dielectric microsphere positioned in water ($n_b = 1.33$) with $r_s = 0.4\,\mu$m and $\varepsilon_s = 2.53$ illuminated by the NVAB at a chosen plane ($z = 10/k$). The force distribution is presented with the magnitudes and directions characterized by the lengths and the directions of white arrows, respectively, and the cases with magnitudes less than 1 pN are not shown. (b) Distribution of the longitudinal force (blue line) for the same particle along the x axis. In both panels, the associated beam profiles are overlapped for reference.

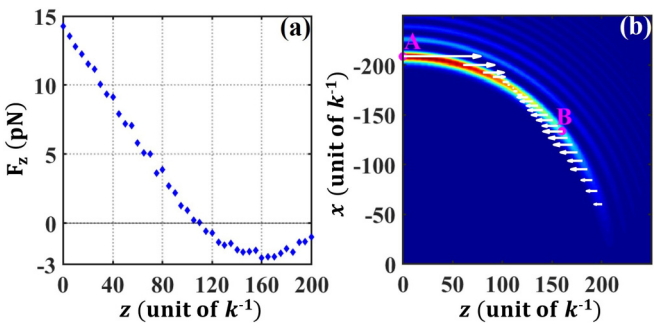

FIG. 3. Longitudinal optical force F_z following the peak intensity of the NVAB along the propagation direction. (a) Calculated values; (b) locations of the forces whose magnitudes (directions) are revealed by the lengths (directions) of white arrows overlapped with the pattern of beam propagation. Sites A and B in panel (b) are the locations corresponding to the maximum pushing and pulling forces, respectively.

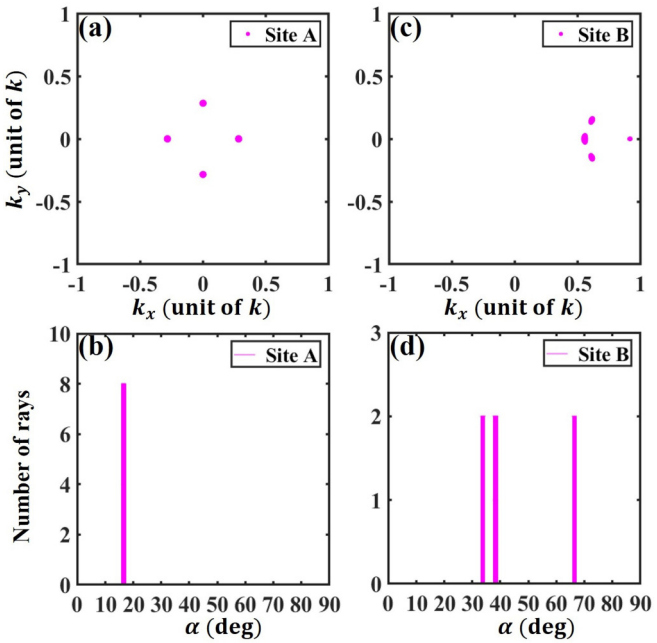

FIG. 4. Optical rays associated with the NVAB passing through sites A and B [marked in Fig. 3(b)] in terms of the spatial frequency (upper) and the angle about the z axis (lower).

for the momentum of the scattered light along the z-axis direction [42] and in turn inducing an optical pulling force ($F_z < 0$) on the particle. Thus, as the accelerating beam bends to a sufficiently large angle, the longitudinal optical force switches from positive to negative values. To have a further understanding of the physical picture behind the pulling effect, we also calculate the scattering pattern corresponding to the case of site B in Fig. 3 where the maximum pulling force appears, and summarize the results in Fig. 5 [where the scattering pattern is obtained by calculating Eq. (A6) in the Appendix]. It is apparent that the forward scatterings are much stronger than the backward scatterings for all directions. This originates from the interferences between particle multipoles that are excited simultaneously [42]. Consequently, the dominant forward scatterings induce a backward force, i.e., the pulling force.

Next, we analyze how the longitudinal optical force coordinates with the transverse trapping to influence the particle movement. To this end, the force is calculated in more detail. Its distribution at several selected propagation distances are presented in Fig. 6. As a result of the beam symmetry about the x axis, the vertical trapping position always appears on this axis where F_y is zero. Typical examples across a location vertically near the peak intensity are shown in Figs. 6(b), 6(f), 6(j), and 6(n). Apparently, F_x (F_y) is always symmetric (antisymmetric). Along the x axis, F_x exhibits an oscillatory shape, matching the feature of the beam pattern. This component is prominent around the main lobe. In this region, the force pointing to the right (i.e., $F_x > 0$) tends to become stronger than the one to the left (i.e., $F_x < 0$) along the beam evolution. For most of the range of propagation (say, $z < 189/k$), the main lobe exhibits a transverse trapping effect very close to the location of the peak intensity. In these associated trapping positions, the longitudinal force is always positive. The pulling force only exists for the beam to turn to large angle and prefers to appear at the left side of the main lobe, nonoverlapping with the transverse trapping position. Thus, in the case of tight transverse trapping, there is no chance for the particle to experience the pulling effect. Such a pulling effect may come into play for loose trapping (e.g., as realized by using a mild beam intensity). Under this condition, the particle probably wanders in the trapping potential upon some external perturbations and enters into the region of the pulling force. This scenario enables fruitful particle movements in the framework of the position-dependent sign of the longitudinal force. For a quite longer propagation distance, the pulling force tends to be comparable to the pushing force and to the transverse force in terms of strength. Thus, one can expect that the pulling effect exerts a greater influence on the particle.

For particles of larger radii, the range of the pulling effect along the propagation becomes short. Here, an example for $r_s = 1\ \mu$m is shown in Fig. 7. At $z = 130/k$, the negative

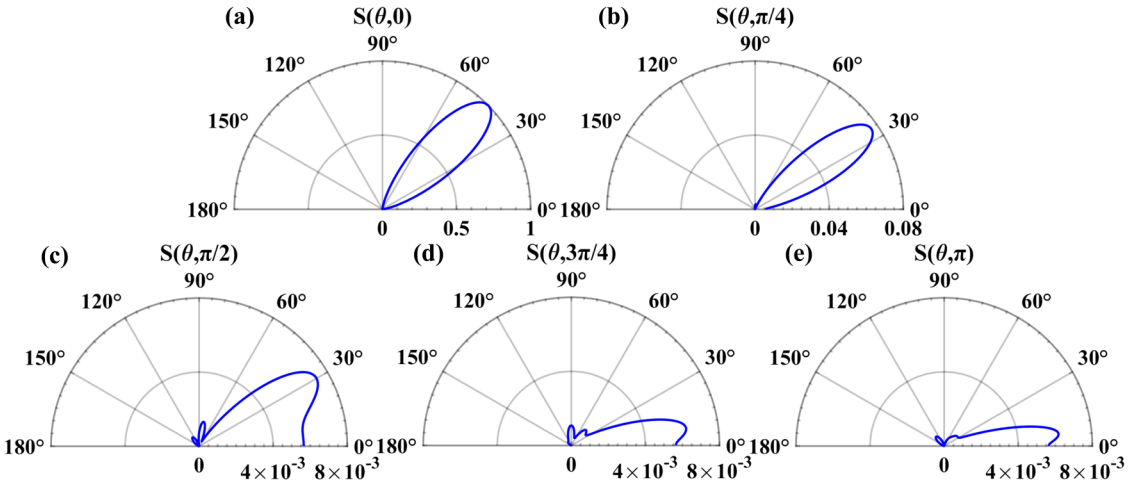

FIG. 5. Normalized scattering intensities $\mathbf{S}(\theta, \phi)$ for a particle with $r_s = 0.4\,\mu$m placed at site B of Fig. 3. Panels (a)–(e) correspond to different azimuthal angles.

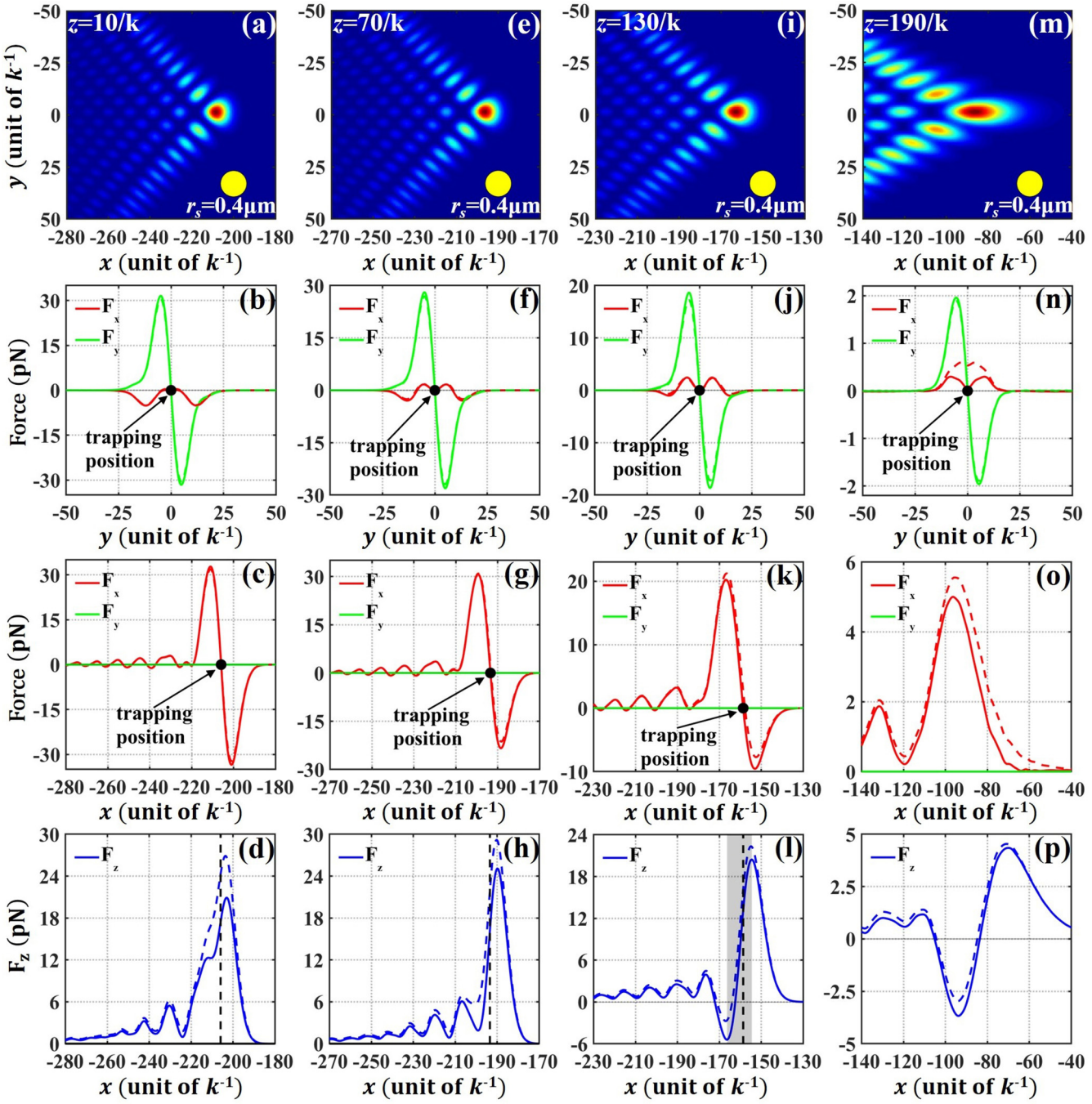

FIG. 6. Optical force experienced by a particle of $r_s = 0.4\ \mu$m in the NVAB. From left to right each panel corresponds to different distances. Shown from upper to lower rows are the transverse beam patterns, the transverse force along a vertical line (near the beam peak intensity) and along the x axis, and the longitudinal force on the x axis. Solid and dashed curved lines in the bottom three rows correspond to $\varepsilon_s = 2.53$ and $\varepsilon_s = 2.53{+}0.01i$, respectively. For the lossless case: the black dots in the second and third rows and the black vertical dashed lines in the bottom row mark the transverse trapping position, while the shaded region in panel (l) shows the range of the trapping potential in panel (k).

longitudinal force is still absent [Fig. 7(a)] while it is already apparent in the former case for this distance. Further simulations reveal that the pulling force indeed initially appears at a much longer distance, i.e., at $z = 170/k$. The weakened pulling effect is also shown by the strength and the location of the pulling force. On the one hand, even for sufficiently large bending of the beam (say, at $z = 190/k$), the magnitude of this force is much smaller than that of the pushing force [Fig. 7(b)]. On the other hand, the pulling force appears further away from the transverse trapping position compared to the case of using a small particle. In contrast to the reduced pulling range, the transverse trapping is extended along the propagation. Particularly, a trapping position even appears near the end of the beam trajectory [Fig. 7(b)]. Based on the above analysis, one can see that the pulling effect is not obvious in the NVAB for particles with a large size, and

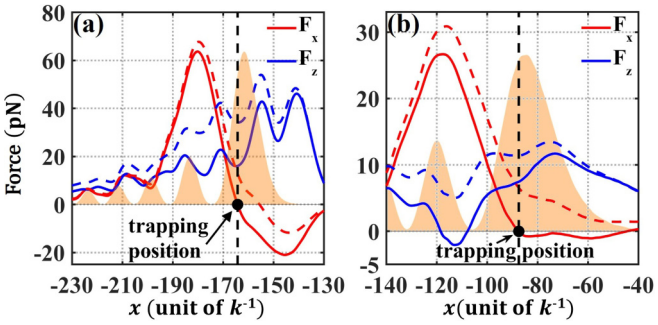

FIG. 7. Optical force experienced by a particle of $r_s = 1\ \mu$m in the NVAB. Transverse (F_x) and longitudinal (F_z) forces are calculated at two selected distances: (a) $z = 130/k$, (b) $z = 190/k$. Solid and dashed curved lines correspond to $\varepsilon_s = 2.53$ and $\varepsilon_s = 2.53{+}0.01i$, respectively. For the lossless case: black dots mark the transverse trapping position. The associated beam profiles (shaded areas) are overlapped for reference.

the beam is mainly functionalized for unidirectional particle delivery along a curved path.

Furthermore, we study the case of particles smaller than the Mie particle employed in Fig. 6 and find a more notable pulling effect. As an example, a Rayleigh polystyrene particle ($r_s = 20$ nm) is considered. The forces experienced by this particle are presented in Fig. 8. Through a direct comparison with the forces for the Mie particle (in the bottom two rows of Fig. 6), one can observe an enhanced pulling effect around the main lobe, i.e., the pulling force is comparable to the pushing force in a longer longitudinal range. In particular, the transverse trapping position falls into the region of pulling force, enabling a stable drag of the Rayleigh particle by the NVAB for a certain distance. Besides, for such a small particle, the sublobes of the NVAB exert considerable contributions to both the transverse and longitudinal forces: stable trapping position and pulling force also appear in the regions of the sublobes, which may bring about more fruitful dynamics for manipulating Rayleigh particles via NVABs.

Finally, we calculate the force by considering the absorption of a microsphere. To this end, we add a small imaginary part that was reported and considered in the literature (see, for instance, Ref. [42]) to the polystyrene permittivity. To directly compare with the lossless case, the calculated results,

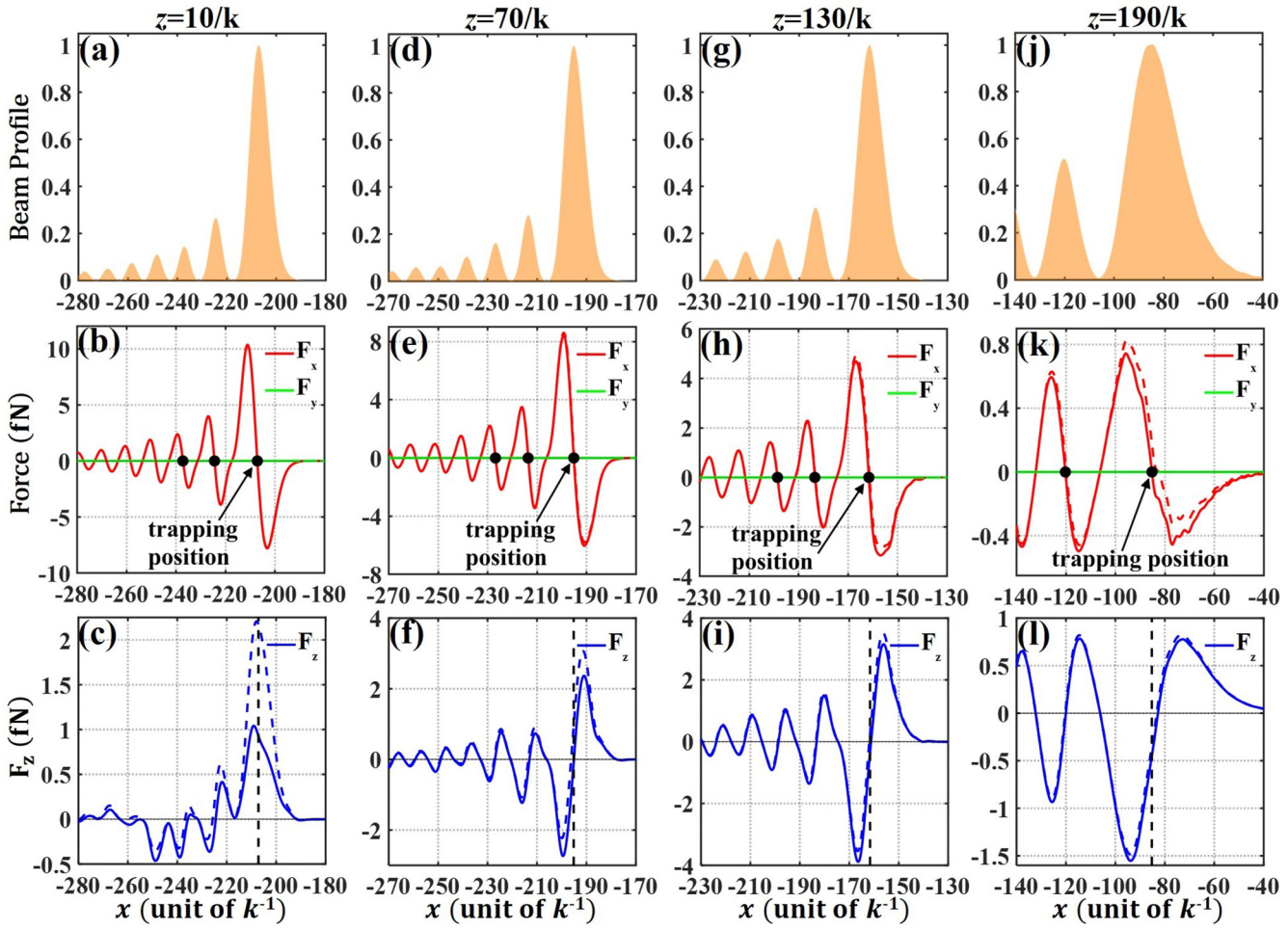

FIG. 8. Optical force experienced by a Rayleigh particle of $r_s = 20$ nm in the NVAB. From left to right each panel corresponds to different distances. Shown from top to bottom rows are the associated beam profiles and the transverse and longitudinal forces on the x axis. Solid and dashed curved lines in the bottom two rows correspond to $\varepsilon_s = 2.53$ and $\varepsilon_s = 2.53{+}0.01i$, respectively. For the lossless case, the black vertical dashed lines in the bottom row mark the dominant transverse trapping positions in the middle row.

plotted by dashed curved lines, are overlapped in Figs. 6–8. Through the comparison, several features appear. First, stable transverse trappings are still achievable, while the associated trapping potentials experience some changes in terms of magnitude and trapping position. Second, the pulling forces are still present, although decreasing in magnitude because the pushing force is enhanced as the microsphere absorbs photons. Third, the difference in terms of forces between the lossy and lossless cases is more apparent for particles with a larger radius.

IV. CONCLUSION

In conclusion, we have studied the forces exerted by an NVAB on a microparticle. The main lobe of the beam dominates the transverse trapping effect yet, surprisingly, the longitudinal force can switch from pushing to pulling type around the main lobe along the propagation. Such an unexpected pulling effect is preferable for the beam turning to large angles and for particles of small size. Around the main lobe, the sign of the longitudinal force also depends on the transverse position. We envision fruitful dynamics of particle trapping and optical manipulations relying on the unique feature of the pulling force arising from these accelerating beams.

ACKNOWLEDGMENTS

The authors are obliged to Dr. Wanli Lu at China University of Mining and Technology for useful discussions. This work was financially supported by the National Key R&D Program of China (2017YFA0303800), the National Natural Science Foundation of China (NSFC) (12022404, 62075105, 91750204), and the 111 Project in China (B07013).

APPENDIX: FORMULATION OF OPTICAL FORCES

To simplify the force calculation, the origin of the coordinate system is set at a particle center. Based on the full-wave generalized Lorenz-Mie theory [55,56], the incident EM field can also be expanded in terms of vector spherical wave functions (VSWFs). In this way, the incident NVAB is expressed as [21,27,56,57]

$$\mathbf{E}_{\rm inc}(r,\theta,\phi) = -i\sum_{n,m} E_{mn}\left[p_{mn}\mathbf{N}^{(1)}_{nm}(k,\mathbf{r}) + q_{mn}\mathbf{M}^{(1)}_{nm}(k,\mathbf{r})\right], \tag{A1}$$

where (r,θ,ϕ) are the spherical coordinates in real space, $\sum_{n,m}$ denotes the summation from $n=1$ to ∞ and from $m=-n$ to n, $E_{mn} = E_0 i^n \gamma_{mn}$ is the coefficient factor with

$$\gamma_{mn} = \left[\frac{(2n+1)(n-m)!}{n(n+1)(n+m)!}\right]^{1/2},$$

and $\mathbf{N}^{(1)}_{nm}(k,\mathbf{r})$ and $\mathbf{M}^{(1)}_{nm}(k,\mathbf{r})$ are the VSWFs. The partial-wave expansion coefficients p_{mn} and q_{mn}, also called beam-shape coefficients, are determined by using the orthogonality of the VSWFs [57]:

$$p_{mn} = \frac{kr}{j_n(kr)}\int_{\theta=0}^{\pi}\int_{\phi=0}^{2\pi}[\mathbf{e}_r\cdot\mathbf{E}_{\rm inc}(\mathbf{r},\theta,\phi)] \times \mathcal{F}_{n,m}(\theta,\phi)\sin\theta d\theta d\phi, \tag{A2a}$$

$$iq_{mn} = -\frac{Zkr}{j_n(kr)}\int_{\theta=0}^{\pi}\int_{\phi=0}^{2\pi}[\mathbf{e}_r\cdot\mathbf{H}_{\rm inc}(\mathbf{r},\theta,\phi)] \times \mathcal{F}_{n,m}(\theta,\phi)\sin\theta d\theta d\phi, \tag{A2b}$$

where j_n denotes a spherical Bessel function of order n, $Z = \sqrt{\mu/\varepsilon}$ stands for the impedance defined by the permittivity ε and the permeability μ in the background, $\mathbf{e}_r$ is the unit vector in the spherical coordinate system, and

$$\mathcal{F}_{n,m}(\theta,\phi) = \frac{i^{1-n}}{\sqrt{4\pi n(n+1)}E_0}Y^*_{n,m}(\theta,\phi), \tag{A3}$$

$$Y^*_{n,m}(\theta,\phi) = \sqrt{\frac{2n+1}{4\pi}\frac{(n-m)!}{(n+m)!}}P^m_n(\cos\theta)e^{-im\phi}, \tag{A4}$$

where $Y^*_{n,m}(\theta,\phi)$ is the complex conjugate of the spherical harmonic function, and $P^m_n(\cos\theta)$ is the associated Legendre function of the first kind. After some algebraic computations involving Eqs. (1), (6), and (A2a), the partial-wave expansion coefficient p_{mn} of the NVAB is simplified as

$$p_{mn} = \frac{\gamma_{mn}}{8\pi^3}\int_{\alpha=0}^{\pi/2}\int_{\beta=0}^{\pi} d\alpha d\beta \frac{e^{im_a f}e^{-im\beta}}{\sin t} \times k^2\sin\alpha\cos\alpha[i\sin\beta\pi_{mn}(\cos\alpha) + \cos\beta\tau_{mn}(\cos\alpha)], \tag{A5a}$$

where $k^2\sin\alpha\cos\alpha d\alpha d\beta = dk_x dk_y$, and $\pi_{mn}(\cos\alpha) = mP^m_n(\cos\alpha)/\sin\alpha$, and $\tau_{mn}(\cos\alpha) = dP^m_n(\cos\alpha)/d\alpha$ are two auxiliary functions. Similarly, for the partial-wave expansion coefficient q_{mn}, one can obtain its simplified expression with the help of Eqs. (4) and (A2b):

$$q_{mn} = \frac{\gamma_{mn}}{8\pi^3}\int_{\alpha=0}^{\pi/2}\int_{\beta=0}^{\pi} d\alpha d\beta \frac{e^{im_a f}e^{-im\beta}}{\sin t} \times k^2\sin\alpha\cos\alpha[i\sin\beta\tau_{mn}(\cos\alpha) + \cos\beta\pi_{mn}(\cos\alpha)]. \tag{A5b}$$

For the scattered EM field, it can be also described via the VSWFs $\mathbf{N}^{(3)}_{nm}(k,\mathbf{r})$ and $\mathbf{M}^{(3)}_{nm}(k,\mathbf{r})$ [21,27,56,57]:

$$\mathbf{E}_{\rm sca}(r,\theta,\phi) = i\sum_{n,m} E_{mn}\left[a_{mn}\mathbf{N}^{(3)}_{nm}(k,\mathbf{r}) + b_{mn}\mathbf{M}^{(3)}_{nm}(k,\mathbf{r})\right], \tag{A6}$$

where a_{mn} and b_{mn} are the partial-wave expansion coefficients of the scattered field. They are readily obtained though the relationships $a_{mn} = a_n p_{mn}$, $b_{mn} = b_n q_{mn}$ with a_n and b_n being the Mie coefficients [55].

The total time-averaged optical force acting on a spherical particle can be evaluated via the integral of Maxwell's stress tensor over the surface S of the particle, which takes the following form [58–60]:

$$\mathbf{F} = \oint_S \hat{\mathbf{n}}\cdot\langle\overleftrightarrow{\mathbf{T}}\rangle dS, \tag{A7}$$

where $\hat{\mathbf{n}}$ is the unit normal vector on the closed surface and the time-averaged Maxwell stress tensor reads

$$\langle\overleftrightarrow{\mathbf{T}}\rangle = \frac{1}{2}\mathrm{Re}\left[\varepsilon\mathbf{E}_t\mathbf{E}_t^* + \mu\mathbf{H}_t\mathbf{H}_t^* - \frac{1}{2}(\varepsilon\mathbf{E}_t\cdot\mathbf{E}_t^* + \mu\mathbf{H}_t\cdot\mathbf{H}_t^*)\overleftrightarrow{\mathbf{I}}\right], \tag{A8}$$

with $\mathbf{E}_t = \mathbf{E}_{\rm inc} + \mathbf{E}_{\rm sca}$ and $\mathbf{H}_t = \mathbf{H}_{\rm inc} + \mathbf{H}_{\rm sca}$ being the total electric and magnetic fields outside the particle, respectively, and $\overleftrightarrow{\mathbf{I}}$ being a unit tensor. Relying on the principle of momentum conservation and the asymptotic form of the Riccati-Bessel function [55], the three components of an optical force can be expressed in terms of the partial-wave expansion coefficients under lossless conditions [21,27,57]:

$$F_x = \mathrm{Re}[F_1], \quad F_y = \mathrm{Im}[F_1], \quad F_z = \mathrm{Re}[F_2], \tag{A9}$$

where

$$F_1 = \frac{2\pi\varepsilon}{k^2}|E_0|^2 \sum_{n,m}\left[c_{11}F_1^{(1)} - c_{12}F_1^{(2)} + c_{13}F_1^{(3)}\right],$$
$$F_2 = -\frac{4\pi\varepsilon}{k^2}|E_0|^2 \sum_{n,m}\left[c_{21}F_2^{(1)} + c_{22}F_2^{(2)}\right], \tag{A10}$$

with the coefficients being

$$c_{11} = \left[\frac{(n-m)(n+m+1)}{n^2(n+1)^2}\right]^{1/2},$$
$$c_{12} = \left[\frac{n(n+2)(n+m+1)(n+m+2)}{(n+1)^2(2n+1)(2n+3)}\right]^{1/2},$$
$$c_{13} = \left[\frac{n(n+2)(n-m)(n-m+1)}{(n+1)^2(2n+1)(2n+3)}\right]^{1/2},$$
$$c_{21} = \left[\frac{n(n+2)(n-m+1)(n+m+1)}{(n+1)^2(2n+1)(2n+3)}\right]^{1/2},$$
$$c_{22} = \frac{m}{n(n+1)}, \tag{A11}$$

and

$$F_1^{(1)} = \tilde{a}_{mn}\tilde{b}^*_{m_1 n} + \tilde{b}_{mn}\tilde{a}^*_{m_1 n} - \tilde{p}_{mn}\tilde{q}^*_{m_1 n} - \tilde{q}_{mn}\tilde{p}^*_{m_1 n},$$
$$F_1^{(2)} = \tilde{a}_{mn}\tilde{a}^*_{m_1 n_1} + \tilde{b}_{mn}\tilde{b}^*_{m_1 n_1} - \tilde{p}_{mn}\tilde{p}^*_{m_1 n_1} - \tilde{q}_{mn}\tilde{q}^*_{m_1 n_1},$$
$$F_1^{(3)} = \tilde{a}_{mn_1}\tilde{a}^*_{m_1 n} + \tilde{b}_{mn_1}\tilde{b}^*_{m_1 n} - \tilde{p}_{mn_1}\tilde{p}^*_{m_1 n} - \tilde{q}_{mn_1}\tilde{q}^*_{m_1 n},$$
$$F_2^{(1)} = \tilde{a}_{mn}\tilde{a}^*_{mn_1} + \tilde{b}_{mn}\tilde{b}^*_{mn_1} - \tilde{p}_{mn}\tilde{p}^*_{mn_1} - \tilde{q}_{mn}\tilde{q}^*_{mn_1},$$
$$F_2^{(2)} = \tilde{a}_{mn}\tilde{b}^*_{mn} - \tilde{p}_{mn}\tilde{q}^*_{mn}, \tag{A12}$$

where the index $m_1 = m + 1$ and $n_1 = n + 1$, and

$$\tilde{a}_{mn} = a_{mn} - \tfrac{1}{2}p_{mn}, \quad \tilde{p}_{mn} = \tfrac{1}{2}p_{mn},$$
$$\tilde{b}_{mn} = b_{mn} - \tfrac{1}{2}q_{mn}, \quad \tilde{q}_{mn} = \tfrac{1}{2}q_{mn}. \tag{A13}$$

[1] Y. Hu, G. A. Siviloglou, P. Zhang, N. K. Efremidis, D. N. Christodoulides, and Z. Chen, *Self-Accelerating Airy Beams: Generation, Control, and Applications* (Springer, New York, 2012), p. 1.

[2] N. K. Efremidis, Z. Chen, M. Segev, and D. N. Christodoulides, Optica **6**, 686 (2019).

[3] J. Baumgartl, M. Mazilu, and K. Dholakia, Nat. Photonics **2**, 675 (2008).

[4] M. Clerici, Y. Hu, P. Lassonde, C. Milián, A. Couairon, D. N. Christodoulides, Z. Chen, L. Razzari, F. Vidal, D. Faccio F. Légaré, and R. Morandotti, Sci. Adv. **1**, e1400111 (2015).

[5] P. Polynkin, M. Kolesik, J. V. Moloney, G. A. Siviloglou, and D. N. Christodoulides, Science **324**, 229 (2009).

[6] P. Polynkin, M. Kolesik, and J. Moloney, Phys. Rev. Lett. **103**, 123902 (2009).

[7] I. Kaminer, M. Segev, and D. N. Christodoulides, Phys. Rev. Lett. **106**, 213903 (2011).

[8] I. Dolev, I. Kaminer, A. Shapira, M. Segev, and A. Arie, Phys. Rev. Lett. **108**, 113903 (2012).

[9] M. Henstridge, C. Pfeiffer, D. Wang, A. Boltasseva, V. M. Shalaev, A. Grbic, and R. Merlin, Science **362**, 439 (2018).

[10] Z. Li, P. Zhang, X. Mu, P. Jia, Y. Hu, Z. Chen, and J. Xu, Photon. Res. **7**, 1087 (2019).

[11] J. X. Li, X. L. Fan, W. P. Zang, and J. G. Tian, Opt. Lett. **36**, 648 (2011).

[12] G. A. Siviloglou and D. N. Christodoulides, Opt. Lett. **32**, 979 (2007).

[13] G. A. Siviloglou, J. Broky, A. Dogariu, and D. N. Christodoulides, Phys. Rev. Lett. **99**, 213901 (2007).

[14] J. Baumgartl, G. M. Hannappel, D. J. Stevenson, D. Day, M. Gu, and K. Dholakia, Lab Chip **9**, 1334 (2009).

[15] H. Cheng, W. Zang, W. Zhou, and J. Tian, Opt. Express **18**, 20384 (2010).

[16] Z. Zheng, B.-F. Zhang, H. Chen, J. Ding, and H.-T. Wang, Appl. Opt. **50**, 43 (2011).

[17] P. Zhang, J. Prakash, Z. Zhang, M. S. Mills, N. K. Efremidis, D. N. Christodoulides, and Z. Chen, Opt. Lett. **36**, 2883 (2011).

[18] W. Lu, J. Chen, Z. Lin, and S. Liu, Prog. Electromagn. Res. **115**, 409 (2011).

[19] J. Zhao, I. D. Chremmos, D. Song, D. N. Christodoulides, N. K. Efremidis, and Z. Chen, Sci. Rep. **5**, 12086 (2015).

[20] Z. Zhao, W. Zang, and J. Tian, J. Opt. **18**, 025607 (2016).

[21] W. Lu, H. Chen, S. Liu, and Z. Lin, Opt. Express **25**, 23238 (2017).

[22] F. G. Mitri, Appl. Phys. Lett. **110**, 181112 (2017).

[23] F. G. Mitri, Eur. Phys. J. D **72**, 21 (2018).

[24] N. Song, R. Li, H. Sun, J. Zhang, B. Wei, S. Zhang, and F. G. Mitri, J. Quant. Spectrosc. Radiat. Transfer **225**, 84 (2020).

[25] Y. Jiang, K. Huang, and X. Lu, Opt. Express **21**, 24413 (2013).

[26] Y. Jiang, Z. Cao, H. Shao, W. Zheng, B. Zeng, and X. Lu, Opt. Express **24**, 18072 (2016).

[27] W. Lu, X. Sun, H. Chen, S. Liu, and Z. Lin, Phys. Rev. A **99**, 013817 (2019).

[28] R. A. B. Suarez, A. A. R. Neves, and M. R. R. Gesualdi, Opt. Laser Technol. **135**, 106678 (2021).

[29] I. Kaminer, R. Bekenstein, J. Nemirovsky, and M. Segev, Phys. Rev. Lett. **108**, 163901 (2012).

[30] F. Courvoisier, A. Mathis, L. Froehly, R. Giust, L. Furfaro, P. A. Lacourt, M. Jacquot, and J. M. Dudley, Opt. Lett. **37**, 1736 (2012).

[31] P. Zhang, Y. Hu, D. Cannan, A. Salandrino, T. Li, R. Morandotti, X. Zhang, and Z. Chen, Opt. Lett. **37**, 2820 (2012).
[32] M. A. Bandres and B. M. Rodríguez-Lara, New J. Phys. **15**, 013054 (2013).
[33] P. Zhang, Y. Hu, T. Li, D. Cannan, X. Yin, R. Morandotti, Z. Chen, and X. Zhang, Phys. Rev. Lett. **109**, 193901 (2012).
[34] P. Aleahmad, M.-A. Miri, M. S. Mills, I. Kaminer, M. Segev, and D. N. Christodoulides, Phys. Rev. Lett. **109**, 203902 (2012).
[35] M. A. Alonso and M. A. Bandres, Opt. Lett. **37**, 5175 (2012).
[36] M. A. Bandres, M. A. Alonso, I. Kaminer, and M. Segev, Opt. Express **21**, 13917 (2013).
[37] Y. Yang, S. Yan, X. Yu, M. Li, and B. Yao, Opt. Express **24**, 27683 (2016).
[38] Z. Zeng and D. Zhao, Ann. Phys. **533**, 2000438 (2021).
[39] R. Schley, I. Kaminer, E. Greenfield, R. Bekenstein, Y. Lumer, and M. Segev, Nat. Commun. **5**, 5189 (2014).
[40] H. Li, Y. Cao, L.-M. Zhou, X. Xu, T. Zhu, Y. Shi, C.-W. Qiu, and W. Ding, Adv. Opt. Photon. **12**, 288 (2020).
[41] S. Sukhov and A. Dogariu, Opt. Lett. **35**, 3847 (2010).
[42] J. Chen, J. Ng, Z. Lin, and C. T. Chan, Nat. Photonics **5**, 531 (2011).
[43] A. Novitsky, C.-W. Qiu, and H. Wang, Phys. Rev. Lett. **107**, 203601 (2011).
[44] A. Dogariu, S. Sukhov, and J. J. Sáenz, Nat. Photonics **7**, 24 (2013).
[45] S.-H. Lee, Y. Roichman, and D. G. Grier, Opt. Express **18**, 6988 (2010).
[46] A. Novitsky, C.-W. Qiu, and A. Lavrinenko, Phys. Rev. Lett. **109**, 023902 (2012).
[47] O. Brzobohatý, V. Karásek, M. Šiler, L. Chvátal, T. Čižmár, and P. Zemánek, Nat. Photonics **7**, 123 (2013).
[48] D. B. Ruffner and D. G. Grier, Phys. Rev. Lett. **109**, 163903 (2012).
[49] C. E. M. Démoré, P. M. Dahl, Z. Yang, P. Glynne-Jones, A. Melzer, S. Cochran, M. P. MacDonald, and G. C. Spalding, Phys. Rev. Lett. **112**, 174302 (2014).
[50] W. Ding, T. Zhu, L.-M. Zhou, and C.-W. Qiu, Adv. Photonics **1**, 024001 (2019).
[51] J. W. Goodman, *Introduction to Fourier Optics* (Robert & Company Publishers, Englewood, 2005).
[52] J. Chen, J. Ng, P. Wang, and Z. Lin, Opt. Lett. **35**, 1674 (2010).
[53] L. Li, Y. Jiang, P. Jiang, X. Li, Y. Qiu, P. Jia, Z. Pi, Y. Hu, Z. Chen, and J. Xu, Opt. Express **28**, 17653 (2020).
[54] Y. Hu, D. Bongiovanni, Z. Chen, and R. Morandotti, Phys. Rev. A **88**, 043809 (2013).
[55] C. F. Bohren and D. R. Huffman, *Absorption and Scattering of Light by Small Particles* (John Wiley and Sons: New York, 1983).
[56] G. Gouesbet and G. Gréhan, *Generalized Lorenz-Mie theories* (Springer, Berlin, 2011), and references therein.
[57] J. Chen, J. Ng, S. Liu, and Z. Lin, Phys. Rev. E **80**, 026607 (2009).
[58] J. D. Jackson, *Classical Electrodynamics*, 3rd ed. (John Wiley and Sons, 1999).
[59] A. Zangwill, *Modern Electrodynamics* (Cambridge University Press, 2012).
[60] Q. Ye and H. Lin, Eur. J. Phys. **38**, 045202 (2017).